

Mechanism of luminescent enhancement in Ba₂GdNbO₆:Eu³⁺ perovskite by Li⁺ co-doping

Marcos Vinicius dos Santos Rezende^a, Mario Ernesto Giroldo Valério^b,
Rodolpho Mouta^c, Eduardo Moraes Diniz^c, Carlos William de Araujo
Paschoal^{c,d,e,*}

^a*Departamento de Física, Universidade Federal de Sergipe, 49500-000, Itabaiana-Se, Brazil*

^b*Departamento de Física, Universidade Federal de Sergipe, 49100-000 São Cristóvão-SE, Brasil.*

^c*Departamento de Física, CCET, Universidade Federal do Maranhão, 65085-580, São Luís - MA, Brazil*

^d*Department of Materials Science and Engineering, University of California Berkeley, 94720-1760, Berkeley - CA, United States*

^e*Department of Physics, University of California Berkeley, 94720-7300, Berkeley - CA, United States*

Abstract

We investigated the Li⁺ ion incorporation in Ba₂GdNbO₆:Eu³⁺ perovskite by atomistic simulations based on energy minimization. We predicted the most probable sites occupied by Eu³⁺ and Li⁺ ions and the related charge-compensation mechanisms involved into these substitutions. The results show that the Eu³⁺ and Li⁺ ions are incorporated mainly at the Gd³⁺ site. In the Li⁺ ion case, there is a charge compensation by Nb_{Gd}^{••} antisite. The crystal field parameters and the transition levels for the Eu³⁺ ion in the BGN:Eu³⁺ were calculated with basis on the simulated local symmetry of the Eu³⁺ site. The results show that the mechanism of luminescent properties enhancement is the symmetry distortion induced by the Li⁺ co-doping.

Keywords: Double perovskite; defect calculations; atomistic simulation; luminescence.

*Corresponding author: Phone: +55 98 3272 8222; Fax: +55 98 3272 8204; alternative e-mails: paschoal.william@gmail.com; paschoal.william@berkeley.edu

Email address: paschoal@ufma.br (Carlos William de Araujo Paschoal)

1. Introduction

The Li^+ ion has been extensively introduced into different oxide hosts, such as: $YVO_4 : Eu^{3+}$ [1], $SrAl_2O_4 : Eu^{3+}$ [2], $Y_2O_3 : Eu^{3+}$ [3, 4], $Gd_2O_3 : Eu^{3+}$ [5], $SrZnO_2 : Eu^{3+}$ [6] and perovskite compounds [7, 8, 9] to improve their luminescent properties. Usually, Li^+ ions act as co-activators in these compounds. Moreover, several studies showed that the Li^+ ion addition affects positively the morphology of particles as well as the luminescent efficiency of oxide materials. The improved luminescence intensity can be originated from local crystal field symmetry breaking around the rare-earth ions by the Li^+ doping. Particularly, Eu^{3+} incorporation into Ba_2GdNbO_6 (BGN) matrix modifies the luminescence spectrum due to the creation of emission centers, which generates specific red light [10]. Since Li^+ ion is very small, it can occupy any site in the BGN structure, either substitutionally, at the Ba^{2+} , Gd^{3+} or Nb^{5+} sites, or interstitially. In both cases, to compensate the charge, additional defects are created, which can modify the local crystal field symmetry around the RE ions.

Recently, Liu et al [10] reported a detailed investigation about the synthesis and luminescence characterization of the BGN: Eu^{3+} , Dy^{3+} and Li^+ co-doped BGN: Eu^{3+} , Dy^{3+} samples. They observed that the co-doping enhances the emissions of BGN: Eu^{3+}/Dy^{3+} samples and related this enhancement to the charge compensation mechanism, which plays an important role in improving the luminescence efficiency of phosphors [5, 11, 12].

In this paper we investigated the charge compensation mechanisms due to the Li^+ incorporation into BGN: Eu^{3+} perovskite. We identified, by atomistic modelling and a simple overlap model, the most probable charge compensation mechanisms and the local symmetry breaking induced by Li co-doping, which is the mechanism that enhances the luminescent properties.

2. Computational method

To model the pristine BGN crystal, a standard lattice-energy minimization using the General Utility Lattice Program (GULP) code [13, 14, 15] was performed. Buckingham pairwise potentials were assumed for all interionic interactions, which were described together with the electrostatic interaction in the form:

$$U_{ij}(r_{ij}) = \frac{Z_i Z_j e^2}{r_{ij}} + A_{ij} \exp \left[\frac{-r_{ij}}{\rho_{ij}} \right] - \frac{B_{ij}}{r_{ij}^6}. \quad (1)$$

In this equation, the first term describes the long-range electrostatic interaction between the ions of charge $Z_i e$ and $Z_j e$ separated by the distance r_{ij} ; the second term models the Pauli short-range repulsion and the last term models the van der Waals attraction. To compute the Coulomb term, the Ewald summation [16], which is standard in GULP code, was employed. The barium and oxygen ions were treated by the shell model [17]. In this model is assumed that the i^{th} ion is formed by a massless shell with charge Y_i and a core with mass m_i whose charge is $Z_i e - Y_i e$, with Z_i being the valence of the i^{th} ion. To obtain a finite ionic polarizability the core is connected to the shell by a harmonic spring, whose force constant is k_i . Gd^{3+} , Eu^{3+} and Li^+ ions were modeled using a rigid ion model due to their low polarizability.

The basic point defect energies were calculated using the Mott–Littleton method that considers the point defect in the centre of a region, in which all interactions immediately surrounding it (region I) are treated explicitly, while a continuum approach is used for more distant regions from the defect (region IIb). These two regions are connected by another one region called IIa, in which ions are allowed to relax, but assuming that they are in harmonic potential wells. [18]. Typical region radii of 12 Å (region I) and 16 Å (region IIa) were adopted.

The electronic transitions of the Eu^{3+} ion were calculated using the modified crystal field theory based on the Judd-Ofelt theory [19, 20]. In this theory, the energies are related to the crystal field Hamiltonian (H_{CF}) by:

$$H_{CK} = \sum_{k,q} B_q^k C_q^k \quad (2)$$

In this equation, the C_q^k parameters describe the contribution of the dopant ion to the crystal field Hamiltonian, while the B_q^k parameters describe the corresponding contribution of the Eu^{3+} surrounding oxygen ions. To calculate the B_q^k parameters the simple overlap (SO) model [21] was employed. The initial data used in the SO model were the dopant ion position and the relaxed positions of the surrounding ions, which were obtained by the defect calculations. This method was employed with success to optical transitions for other materials [22, 23, 24].

3. Results

3.1. Potential adopted and basic defect calculations

BGN crystallizes in a tetragonal distorted perovskite that derives from the cubic rock salt double perovskite structure. However, as the tetragonal distortion is small, BGN can be well described by the pseudocubic structure [25, 26]. We assumed a previous complete set of potentials assumed to model the pristine BGN crystal [27, 28, 29], which is listed in Table 1. This potential set exhibits an excellent reliability to model the structural properties of BGN. Besides, the dielectric properties of BGN were remarkably modeled by this potential data, which is a necessary condition for consistent defect calculation [30]. The good reliability of the potential set assumed can be checked comparing the error between calculated and experimental values for structural and dielectric properties of BGN, which are lower than 1%. Table 1 also shows the used interactions for Eu^{3+} [29] and Li^+ , which were took from [27, 29].

Table 1: Short-range potentials parameters assumed to model pristine BGN crystal [29, 28, 27].

Shell model interactions			
Shell-Shell interactions			
Interaction	A/eV	$\rho/\text{\AA}$	$C/\text{eV}\text{\AA}^6$
$\text{Ba}^{2+} - \text{O}^{2-}$	4818.4160	0.30670	0.00
$\text{Nb}^{5+} - \text{O}^{2-}$	1796.30	0.345980	0.00
$\text{O}^{2-} - \text{O}^{2-}$	25.41	0.69370	32.32
Core-Shell interactions			
Ion	$k/\text{eV}\text{\AA}^{-2}$	$Y/ e $	
Ba^{2+}	34.05	1.83100	
Nb^{5+}	1358.58	-4.49700	
O^{2-}	20.53	-2.51300	
Rigid ion model interactions			
Interaction	A/eV	$\rho/\text{\AA}$	$C/\text{eV}\text{\AA}^6$
$\text{Gd}^{3+} - \text{O}^{2-}$	1204.60	0.334137	0.00
$\text{Eu}^{3+} - \text{O}^{2-}$	1156.72	0.337617	0.00
$\text{Li}^+ - \text{O}^{2-}$	426.48	0.3000	0,00

We considered two possible interstitial positions to put each ion, intrinsic or extrinsic, in the pristine BGN crystal, namely: $i_1 = (\frac{1}{4}, \frac{1}{4}, 0)$ and

$i_2 = (\frac{1}{8}, \frac{1}{8}, \frac{1}{8})$, as they are shown in Fig 1. The position i_1 was in xy plane in the square formed by the Nb and RE ions, while the position i_2 was in the diagonal between the Nb and RE ions. In the calculation, it was considered the formation energy of the most probable interstitial position. The formation energies of the basic point defects (vacancies and interstitials), as well as lattice energies, are given in Tables 2 and 3, respectively. We used the KrögerVink notation to label the defects.

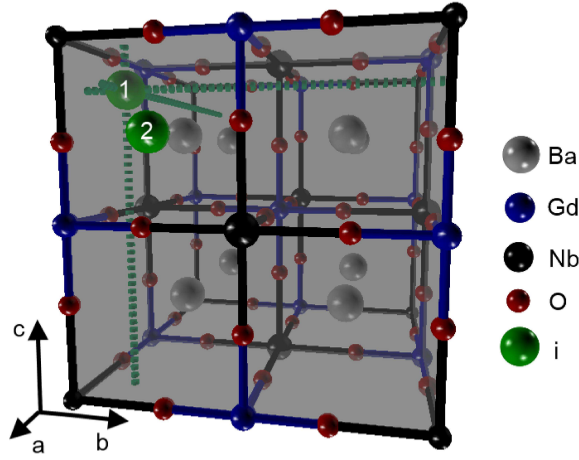


Figure 1: Pseudocubic unit cell of BGN showing the positions $i_1 = (\frac{1}{4}, \frac{1}{4}, 0)$ and $i_2 = (\frac{1}{8}, \frac{1}{8}, \frac{1}{8})$ assumed as interstitial positions in this paper.

The basic defects that involve Nb^{5+} ions, i. e., Nb vacancies (V_{Nb}''''), Nb interstitials ($\text{Nb}_i^{\bullet\bullet\bullet\bullet}$) have higher absolute value of formation energies than those involving other ions (Ba^{2+} , Gd^{3+} and O^{2-}). Besides, the more negative the antisite defect charge is, the more positive is its formation energy (and the opposite is also true). Such behaviours can be explained as follows: each ion has a contribution for the (negative) net lattice energy, which is mainly due to the electrostatic potential. The greater the modulus of its charge, the greater this contribution. Furthermore, because of the energy extensivity, by adding an ion to the crystal, the net lattice energy decreases; by removing it, the net lattice energy increases. Therefore, by creating a Nb vacancy, the contribution loss is greater than by creating any other vacancies, resulting in a more positive net lattice energy; when a Nb interstitial is created, the contribution gain is greater than that of any other interstitial.

Table 2: Formation energy of basic defects in the pristine BGN crystal. $i1 = (\frac{1}{4}, \frac{1}{4}, 0)$ and $i2 = (\frac{1}{8}, \frac{1}{8}, \frac{1}{8})$

Defect	Energy /eV
Vacancies	
V_{Ba}''	20.90
V_{Gd}'''	46.89
V_{Nb}''''	138.53
$V_O^{\bullet\bullet}$	16.34
Interstitials at i_1 position	
$Ba_{i1}^{\bullet\bullet}$	-9.90
$Gd_{i1}^{\bullet\bullet\bullet}$	-33.55
$Nb_{i1}^{\bullet\bullet\bullet\bullet}$	-109.34
O_{i1}''	-7.40
Li_{i1}^{\bullet}	-6.48
Interstitials at i_2 position	
$Ba_{i2}^{\bullet\bullet}$	-9.70
$Gd_{i2}^{\bullet\bullet\bullet}$	-31.87
$Nb_{i2}^{\bullet\bullet\bullet\bullet}$	-106.28
O_{i2}''	-6.84
Li_{i2}^{\bullet}	-5.31
Substitution energies in BGN	
$Nb_{Gd}^{\bullet\bullet}$	-83.51
$Nb_{Ba}^{\bullet\bullet\bullet}$	-92.45
Ba_{Nb}'''	116.45
Ba_{Gd}'	25.62
Gd_{Ba}^{\bullet}	-20.62
Gd_{Nb}''	88.49
Eu_{Ba}^{\bullet}	-20.52
Eu_{Gd}''	0.15
Eu_{Nb}''	88.65
Li_{Ba}'	12.90
Li_{Gd}''	36.89
Li_{Nb}''''	127.41

Table 3: Calculated lattice energies for the pristine BGN crystal and the start oxides.

Compound	E_{latt} / eV
BGN	-297.63
BaO	-32.18
Gd_2O_3	-129.56
Nb_2O_5	-323.72
Li_2O	-30.51
Eu_2O_3	-129.28

As for antisites, when we replace an ion by another one with lower charge, we reduce the contribution, increasing the net lattice energy. The opposite is also true: more positively charged antisites must have a more negative formation energy. That is also the reason why the antisite Eu_{Gd} , whose charge is null, has the lower energy of all. Thus, it is evident that our results are in complete agreement to what one should expect for the basic defect formation energies.

3.2. Eu^{3+} inclusion

As the Eu^{3+} ion is a trivalent lanthanide, it is expected it occupies substitutionally the Gd^{3+} site without charge compensation. However, all other possible defect configurations cannot be discarded, i. e., the incorporation into the Ba^{2+} and Nb^{5+} sites also need to be evaluated. It is important to point out that the incorporation into the Ba^{2+} and Nb^{5+} sites generates more than one possible defects due to different charge compensation mechanisms. We listed all types of defects considered due to the Eu^{3+} inclusion in the pristine BGN crystal and the charge compensation mechanisms associated to them in Table 4. The results confirm that the most probable inclusion of Eu^{3+} is into the Gd^{3+} site.

3.3. Li^+ inclusion

Considering the BGN crystalline structure, the Li^+ ion can be inserted into the Ba^{2+} , Gd^{3+} , Nb^{5+} sites and in the most probable interstice (i_1). For all of them, there are more than one charge-compensating mechanism. We listed all type of defects considered due to the Li^+ inclusion into the pristine BGN crystal and the charge compensation mechanisms associated to them in Table 5. The solution energies (unbound) per defect are also shown.

Table 4: Types of Defects considered due to the Eu^{3+} inclusions in the pritine BGN crystal and solution energies by defect of each reaction in eV.

Site	Charge compensation	Reaction	Energy
Gd^{3+}	No charge compensation	$\frac{1}{2}\text{Eu}_2\text{O}_3 + \text{Gd}_2\text{O}_3 \rightarrow (\text{Eu}_{\text{Gd}}^x) + \frac{1}{2}\text{Gd}_2\text{O}_3$	0.01
Ba^{2+}	Barium vacancies	$\text{Eu}_2\text{O}_3 + 3\text{Ba}_{\text{Ba}}^x \rightarrow (2\text{Eu}_{\text{Ba}}^x + \text{V}_{\text{Ba}}^{\bullet\bullet}) + 3\text{BaO}$	4.20
	Oxygen interstitial	$\text{Eu}_2\text{O}_3 + 2\text{Ba}_{\text{Ba}}^x \rightarrow (2\text{Eu}_{\text{Ba}}^x + \text{O}_i^{\bullet}) + 2\text{BaO}$	5.49
	Gadolinium vacancies	$\frac{3}{2}\text{Eu}_2\text{O}_3 + 3\text{Ba}_{\text{Ba}}^x + \text{Gd}_{\text{Gd}}^x \rightarrow (3\text{Eu}_{\text{Ba}}^x + \text{V}_{\text{Gd}}^{\bullet\bullet}) + 3\text{BaO} + \frac{1}{2}\text{Gd}_2\text{O}_3$	4.48
	Niobium vacancies	$\frac{3}{2}\text{Eu}_2\text{O}_3 + 5\text{Ba}_{\text{Ba}}^x + \text{Nb}_{\text{Nb}}^x \rightarrow (5\text{Eu}_{\text{Ba}}^x + \text{V}_{\text{Nb}}^{\bullet\bullet\bullet}) + 5\text{BaO} + \frac{1}{2}\text{Nb}_2\text{O}_5$	6.06
	Anti-site (Ba_{Gd}^x)	$\frac{1}{2}\text{Eu}_2\text{O}_3 + \text{Ba}_{\text{Ba}}^x + \text{Gd}_{\text{Gd}}^x \rightarrow (\text{Eu}_{\text{Ba}}^x + \text{Ba}_{\text{Gd}}^x) + \frac{1}{2}\text{Gd}_2\text{O}_3$	2.48
	Anti-site (Gd_{Nb}^x)	$\text{Eu}_2\text{O}_3 + 2\text{Ba}_{\text{Ba}}^x + \frac{1}{2}\text{Gd}_2\text{O}_3 \rightarrow (2\text{Eu}_{\text{Ba}}^x + \text{Gd}_{\text{Nb}}^x) + 2\text{BaO} + \frac{1}{2}\text{Nb}_2\text{O}_5$	5.10
	Anti-site (Ba_{Nb}^x)	$\frac{3}{2}\text{Eu}_2\text{O}_3 + 3\text{Ba}_{\text{Ba}}^x + \text{Nb}_{\text{Nb}}^x \rightarrow (3\text{Eu}_{\text{Ba}}^x + \text{Ba}_{\text{Nb}}^x) + 2\text{BaO} + \frac{1}{2}\text{Nb}_2\text{O}_5$	5.65
Nb^{5+}	Oxygen vacancies	$\frac{1}{2}\text{Eu}_2\text{O}_3 + \text{O}_O + \text{Nb}_{\text{Nb}}^x \rightarrow (\text{Eu}_{\text{Nb}}^x + \text{V}_O^{\bullet\bullet}) + \frac{1}{2}\text{Nb}_2\text{O}_5$	3.89
	Barium interstitial	$\frac{1}{2}\text{Eu}_2\text{O}_3 + \text{BaO} + \text{Nb}_{\text{Nb}}^x \rightarrow (\text{Eu}_{\text{Nb}}^x + \text{Ba}_i^{\bullet}) + \frac{1}{2}\text{Nb}_2\text{O}_5$	6.95
	Gadolinium interstitial	$\frac{3}{2}\text{Eu}_2\text{O}_3 + \text{Gd}_2\text{O}_3 + 3\text{Nb}_{\text{Nb}}^x \rightarrow (3\text{Eu}_{\text{Nb}}^x + 2\text{Gd}_i^{\bullet\bullet\bullet}) + \frac{3}{2}\text{Nb}_2\text{O}_5$	7.35
	Niobium interstitial	$\frac{3}{2}\text{Eu}_2\text{O}_3 + 5\text{Nb}_{\text{Nb}}^x \rightarrow (5\text{Eu}_{\text{Nb}}^x + 2\text{Nb}_i^{\bullet\bullet\bullet}) + \frac{3}{2}\text{Nb}_2\text{O}_5$	8.88
	Anti-site ($(\text{Gd}_{\text{Ba}}^x)$)	$\frac{1}{2}\text{Eu}_2\text{O}_3 + 2\text{Ba}_{\text{Ba}}^x + \text{Nb}_{\text{Nb}}^x + \text{Gd}_2\text{O}_3 \rightarrow (5\text{Eu}_{\text{Nb}}^x + 2\text{Gd}_{\text{Ba}}^x) + 2\text{BaO} + \frac{1}{2}\text{Nb}_2\text{O}_5$	5.13
	Anti-site ($(\text{Nb}_{\text{Gd}}^x)$)	$\frac{1}{2}\text{Eu}_2\text{O}_3 + \text{Gd}_{\text{Gd}}^x + \text{Nb}_{\text{Nb}}^x \rightarrow (5\text{Eu}_{\text{Nb}}^x + \text{Nb}_{\text{Gd}}^x) + \frac{1}{2}\text{Gd}_2\text{O}_3$	2.50
	Anti-site ($(\text{Nb}_{\text{Ba}}^x)$)	$\frac{3}{2}\text{Eu}_2\text{O}_3 + \text{Ba}_{\text{Ba}}^x + 3\text{Nb}_{\text{Nb}}^x \rightarrow (3\text{Eu}_{\text{Nb}}^x + 2\text{Nb}_{\text{Ba}}^x) + 2\text{BaO} + \frac{1}{2}\text{Nb}_2\text{O}_5$	9.75

Table 5: Types of Defects considered due to the Li^+ inclusion in the pristine BGN crystal and solution energies by defect of each reaction in eV.

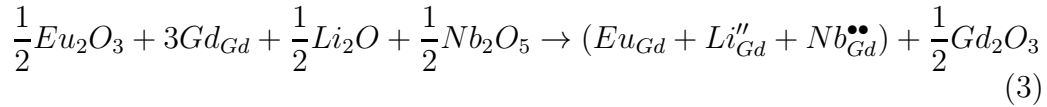
Site	Charge compensation	Reaction	Energy
Gd^{3+}	Oxygen vacancies	$\frac{1}{2}\text{Li}_2\text{O} + \text{O}_O^x + \text{Gd}_{\text{Gd}}^x \rightarrow (\text{Li}_{\text{Gd}}^x + \text{V}_O^{\bullet\bullet}) + \frac{1}{2}\text{Gd}_2\text{O}_3$	1.85
	Barium interstitial	$\frac{1}{2}\text{Li}_2\text{O} + \text{BaO} + \text{Gd}_{\text{Gd}}^x \rightarrow (\text{Li}_{\text{Gd}}^x + \text{Ba}_i^{\bullet}) + \frac{1}{2}\text{Gd}_2\text{O}_3$	4.82
	Gadolinium interstitial	$\frac{3}{2}\text{Li}_2\text{O} + 3\text{Gd}_{\text{Gd}}^x \rightarrow (3\text{Li}_{\text{Gd}}^x + 2\text{Gd}_i^{\bullet\bullet}) + \frac{3}{2}\text{Gd}_2\text{O}_3$	4.91
	Niobium interstitial	$\frac{3}{2}\text{Li}_2\text{O} + 5\text{Gd}_{\text{Gd}}^x + \text{Nb}_2\text{O}_5 \rightarrow (5\text{Li}_{\text{Gd}}^x + 2\text{Nb}_i^{\bullet\bullet\bullet}) + \frac{5}{2}\text{Gd}_2\text{O}_3$	5.98
	Anti-site (Gd_{Ba}^x)	$\frac{1}{2}\text{Li}_2\text{O} + \frac{1}{2}\text{Gd}_2\text{O}_3 + 2\text{Ba}_{\text{Ba}}^x + \text{Gd}_{\text{Gd}}^x \rightarrow (\text{Li}_{\text{Gd}}^x + 2\text{Gd}_{\text{Ba}}^x) + 2\text{BaO}$	10.65
	Anti-site (Nb_{Gd}^x)	$\frac{1}{2}\text{Li}_2\text{O} + 2\text{Gd}_{\text{Gd}}^x + \frac{1}{2}\text{Nb}_2\text{O}_5 \rightarrow (\text{Li}_{\text{Gd}}^x + \text{Nb}_{\text{Gd}}^x) + \frac{1}{2}\text{Gd}_2\text{O}_3$	0.47
	Anti-site (Nb_{Ba}^x)	$\frac{3}{2}\text{Li}_2\text{O} + 3\text{Gd}_{\text{Gd}}^x + 2\text{Ba}_{\text{Ba}}^x + \text{Nb}_2\text{O}_5 \rightarrow (3\text{Li}_{\text{Gd}}^x + 2\text{Nb}_{\text{Ba}}^x) + 2\text{BaO} + \frac{3}{2}\text{Gd}_2\text{O}_3$	7.31
Ba^{2+}	Oxygen vacancies	$\text{Li}_2\text{O} + \text{O}_O^x + \text{Ba}_{\text{Ba}}^x \rightarrow (2\text{Li}_{\text{Ba}}^x + \text{V}_O^{\bullet\bullet}) + 2\text{BaO}$	2.76
	Barium interstitial	$\text{Li}_2\text{O} + 2\text{Ba}_{\text{Ba}}^x \rightarrow (\text{Li}_{\text{Ba}}^x + \text{Ba}_i^{\bullet}) + \text{BaO}$	4.74
	Gadolinium interstitial	$\frac{1}{2}\text{Li}_2\text{O} + 3\text{Ba}_{\text{Ba}}^x + \frac{1}{2}\text{Gd}_2\text{O}_3 \rightarrow (3\text{Li}_{\text{Ba}}^x + \text{Gd}_i^{\bullet\bullet\bullet}) + 3\text{BaO}$	4.79
	Niobium interstitial	$\frac{1}{2}\text{Li}_2\text{O} + 5\text{Ba}_{\text{Ba}}^x + \frac{1}{2}\text{Nb}_2\text{O}_5 \rightarrow (5\text{Li}_{\text{Ba}}^x + \text{Nb}_i^{\bullet\bullet\bullet}) + 5\text{BaO}$	5.40
	Anti-site (Gd_{Ba}^x)	$\frac{1}{2}\text{Li}_2\text{O} + 2\text{Ba}_{\text{Ba}}^x + \frac{1}{2}\text{Gd}_2\text{O}_3 \rightarrow (\text{Li}_{\text{Ba}}^x + \text{Gd}_{\text{Ba}}^x) + 2\text{BaO}$	3.98
	Anti-site (Nb_{Gd}^x)	$\text{Li}_2\text{O} + 2\text{Ba}_{\text{Ba}}^x + \text{Gd}_{\text{Gd}}^x + \frac{1}{2}\text{Nb}_2\text{O}_5 \rightarrow (2\text{Li}_{\text{Ba}}^x + \text{Nb}_{\text{Gd}}^x) + 2\text{BaO} + \frac{1}{2}\text{Gd}_2\text{O}_3$	1.84
	Anti-site (Nb_{Ba}^x)	$\frac{3}{2}\text{Li}_2\text{O} + 4\text{Ba}_{\text{Ba}}^x + \frac{1}{2}\text{Nb}_2\text{O}_5 \rightarrow (3\text{Li}_{\text{Ba}}^x + \text{Nb}_{\text{Ba}}^x) + 4\text{BaO}$	2.48
Nb^{5+}	Oxygen vacancies	$\frac{1}{2}\text{Li}_2\text{O}_2 + \text{O}_O^x + \text{Nb}_{\text{Nb}}^x \rightarrow (\text{Li}_{\text{Nb}}^x + 2\text{V}_O^{\bullet\bullet}) + \frac{1}{2}\text{Nb}_2\text{O}_5$	4.50
	Barium interstitial	$\frac{1}{2}\text{Li}_2\text{O}_2 + \text{BaO} + \text{Nb}_{\text{Nb}}^x \rightarrow (\text{Li}_{\text{Nb}}^x + 2\text{Ba}_i^{\bullet}) + \frac{1}{2}\text{Nb}_2\text{O}_5$	8.46
	Gadolinium interstitial	$\frac{3}{2}\text{Li}_2\text{O} + 3\text{Nb}_{\text{Nb}}^x + 2\text{Gd}_2\text{O}_3 \rightarrow (3\text{Li}_{\text{Nb}}^x + 4\text{Gd}_i^{\bullet\bullet\bullet}) + \frac{3}{2}\text{Nb}_2\text{O}_5$	9.62
	Niobium interstitial	$\frac{3}{2}\text{Li}_2\text{O} + 5\text{Nb}_{\text{Nb}}^x \rightarrow (5\text{Li}_{\text{Nb}}^x + 4\text{Nb}_i^{\bullet\bullet\bullet}) + \frac{1}{2}\text{Nb}_2\text{O}_5$	12.68
	Anti-site (Gd_{Ba}^x)	$\frac{1}{2}\text{Li}_2\text{O} + 4\text{Ba}_{\text{Ba}}^x + \frac{1}{2}\text{Gd}_2\text{O}_3 \rightarrow (\text{Li}_{\text{Nb}}^x + 4\text{Gd}_{\text{Ba}}^x) + 4\text{BaO} + \frac{1}{2}\text{Nb}_2\text{O}_5$	5.74
	Anti-site (Nb_{Gd}^x)	$\frac{1}{2}\text{Li}_2\text{O} + \text{Nb}_{\text{Nb}}^x + 2\text{Gd}_{\text{Gd}}^x + \frac{1}{2}\text{Nb}_2\text{O}_5 \rightarrow (\text{Li}_{\text{Nb}}^x + 2\text{Nb}_{\text{Gd}}^x) + \text{Gd}_2\text{O}_3$	2.65
	Anti-site (Nb_{Ba}^x)	$\frac{3}{2}\text{Li}_2\text{O} + 3\text{Nb}_{\text{Nb}}^x + 4\text{Ba}_{\text{Ba}}^x + \frac{1}{2}\text{Nb}_2\text{O}_5 \rightarrow (3\text{Li}_{\text{Nb}}^x + 4\text{Nb}_{\text{Ba}}^x) + 4\text{BaO}$	13.05
Interstitial	Barium vacancies	$\text{Li}_2\text{O} + \text{Ba}_{\text{Ba}}^x \rightarrow (2\text{Li}_i^x + \text{V}_{\text{Ba}}^{\bullet\bullet}) + \text{BaO}$	2.09
	Oxygen interstitial	$\text{Li}_2\text{O} \rightarrow (2\text{Li}_i^x + \text{O}_i^{\bullet})$	3.38
	Gadolinium vacancies	$\frac{3}{2}\text{Li}_2\text{O} + \text{Gd}_{\text{Gd}}^x \rightarrow (3\text{Li}_i^x + \text{V}_{\text{Gd}}^{\bullet\bullet}) + \frac{1}{2}\text{Gd}_2\text{O}_3$	2.11
	Niobium vacancies	$\frac{3}{2}\text{Li}_2\text{O} + \text{Nb}_{\text{Nb}}^x \rightarrow (5\text{Li}_i^x + \text{V}_{\text{Nb}}^{\bullet\bullet\bullet}) + \frac{1}{2}\text{Nb}_2\text{O}_5$	3.42
	Anti-site (Ba_{Gd}^x)	$\frac{1}{2}\text{Li}_2\text{O} + \text{BaO} + \text{Gd}_{\text{Gd}}^x \rightarrow (\text{Li}_i^x + \text{Ba}_{\text{Gd}}^x) + \frac{1}{2}\text{Gd}_2\text{O}_3$	0.90
	Anti-site (Gd_{Nb}^x)	$\text{Li}_2\text{O} + \frac{1}{2}\text{Gd}_2\text{O}_3 + \text{Nb}_{\text{Nb}}^x \rightarrow (2\text{Li}_i^x + \text{Gd}_{\text{Nb}}^x) + \frac{1}{2}\text{Nb}_2\text{O}_5$	4.48
	Anti-site (Ba_{Nb}^x)	$\frac{3}{2}\text{Li}_2\text{O} + \text{BaO} + \text{Nb}_{\text{Nb}}^x \rightarrow (3\text{Li}_i^x + \text{Ba}_{\text{Nb}}^x) + \frac{1}{2}\text{Nb}_2\text{O}_5$	3.27

According to the results, there is an energetic preference for the Li^+ incorporation into the Gd^{3+} site compensated by $\text{Nb}_{\text{Gd}}^{\bullet\bullet}$ antisite, whose solution energy is 0.47 eV. The following energetic preferences are: the incorporation into the interstitial site i_1 , compensated by Ba'_{Gd} antisite, with a solution energy of 0.90 eV; the Ba^{2+} site, compensated by $\text{Nb}_{\text{Gd}}^{\bullet\bullet}$ antisite, with a solution energy of 1.84 eV; and into the Nb^{5+} site, compensated by oxygen vacancies, with an energy of 1.85 eV.

It is important to point out that we calculated the bound solution energies. The unbound solution assumes that there is no interaction between dopant and charge-compensating defect, while in the bound solution, the calculations are carried out for a configuration consisting of the dopant and charge-compensating defects in vicinity positions, meaning that the energies include the contribution of the binding energy of the defect. The reason for including the bound solution energies was to perform a careful analysis of the relaxed configurations, which revealed the large distortions in the surrounding lattice caused by the Li^+ co-dopant and the charge-compensating defect required to keep the total charge neutral close to the Eu^{3+} ion. The presence of a charge-compensating defect near the active centre can change the local symmetry of the active centre and, therefore, change the luminescence efficiency of phosphors.

3.4. Simultaneous Eu^{3+} and Li^+ inclusions

To explain how the Li^+ co-doping enhances the luminescence efficiency of $\text{BGN}:\text{Eu}^{3+}$, as reported by Yu et al. [10], we calculated the incorporation of Eu^{3+} and Li^+ simultaneously into BGN crystal. According to Yu et al, Li^+ co-doping helps to incorporate Eu^{3+} and Dy^{3+} into lattice sites by increasing the crystallinity. We considered only those configurations more favorable to incorporate the dopants and co-dopants in the BGN matrix, with basis on the previous results showed in Tables 4 and 5. Besides, by considering different charge compensation mechanisms, we also tested possible no symmetry configuration of dopant in the matrix. Thus, we considered the Eu^{3+} ion as dopant and the Li^+ ion as co-dopant, and we assumed that there exists a binding energy among both and the charge compensation defect. The reaction that describes these substitutions is:



For the bounded defect, the dopant, co-dopant and charge mechanism can be arranged in six non-equivalent arrangements (C1 to C6), as it is shown in Table 6, which also lists the calculated defect formation and solution energies of the simultaneous Eu^{3+} and Li^+ incorporations into the pristine BGN crystal for each one of the six no equivalent arrangements. According to the results there is a small difference between all configurations. The C6 configuration exhibits the lower energy value, being the most probable configuration.

Configuration	Ion positions			Formation energy / eV	Solution energy / eV
C1	$\text{Eu} \rightarrow (0, 0, 0)$	$\text{Li} \rightarrow (\frac{1}{2}, 0, \frac{1}{2})$	$\text{Nb} \rightarrow (1, 0, 0)$	-47.42	0.00
C2	$\text{Eu} \rightarrow (1, 0, 0)$	$\text{Li} \rightarrow (0, 0, 0)$	$\text{Nb} \rightarrow (\frac{1}{2}, 0, \frac{1}{2})$	-47.35	0.02
C3	$\text{Eu} \rightarrow (\frac{1}{2}, 0, \frac{1}{2})$	$\text{Li} \rightarrow (1, 0, 0)$	$\text{Nb} \rightarrow (0, 0, 0)$	-47.44	-0.01
C4	$\text{Eu} \rightarrow (0, 0, 0)$	$\text{Li} \rightarrow (\frac{1}{2}, 0, \frac{1}{2})$	$\text{Nb} \rightarrow (1, 0, 1)$	-47.17	0.08
C5	$\text{Eu} \rightarrow (1, 0, 1)$	$\text{Li} \rightarrow (0, 0, 0)$	$\text{Nb} \rightarrow (\frac{1}{2}, 0, \frac{1}{2})$	-47.27	0.05
C6	$\text{Eu} \rightarrow (\frac{1}{2}, 0, \frac{1}{2})$	$\text{Li} \rightarrow (1, 0, 1)$	$\text{Nb} \rightarrow (0, 0, 0)$	-47.97	-0.19

Table 6: Possible arrangements of the dopant, co-dopant and charge compensation defect in pristine BGN crystal and respective formation and solution energies.

As previously mentioned, the Li^+ ion co-doping induces lattice distortions in the BGN:Eu^{3+} crystal, and this distortion results in a different crystalline field around the active ion. From the defect calculations we obtained the relaxed positions of Li^+ and Eu^{3+} ions and the respective surrounding lattice ions. We used these positions as initial data to calculate the crystal field parameters B_q^k , which are shown in Table 7 for BGN:Eu^{3+} pure and Li co-doped. The B_q^k parameters provide an unambiguous indication of the local symmetry of the optically active centre in the material and helped to explain the observed system optical activity. The change in local symmetry around the Eu^{3+} ion is in agreement with the variation in the intensity of the electric dipole and magnetic dipole transitions [31, 32]. For the non co-doped BGN:Eu^{3+} , vanishing B_0^k values indicate that the site occupied by the Eu^{3+} ion has high symmetry. Thus, it is expected that the magnetic dipole transition $^5D_0 \rightarrow ^7F_1$ of Eu^{3+} dominates the BGN:Eu^{3+} emission spectra, which is in excellent agreement with the emission spectra reported by Yu et al. [10].

In the $\text{BGN:Eu}^{3+}, \text{Li}^+$ crystal, all B_q^k parameters have a non-zero value, which indicates the Eu^{3+} site symmetry is rather low. The low symmetry is caused by a large deformation resulting from the incorporation of Eu^{3+} into the lattice, the presence of the Li^+ co-dopant and the $\text{Nb}_{Gd}^{\bullet\bullet}$ antisite, all close to the Eu^{3+} ion. This low symmetry implies that the co-doped crystal has more effective luminescence emission than the pure BGN:Eu^{3+} crystal.

The luminescence intensity ratio (R) of ${}^5D_0 \rightarrow {}^7F_1$ and ${}^5D_0 \rightarrow {}^7F_2$ transitions, also called asymmetry ratio, is widely used as an indication of the degree of asymmetry in the vicinity of Eu^{3+} ions [33]. From a comparison of the emission spectra of BGN:Eu^{3+} and $\text{BGN:Eu}^{3+},\text{Li}^+$ crystals, reported by Yu et al. [10], it was noted that the ratio R changed due to the Li^+ co-doping. The greater intensity ratio corresponds to a more distorted or asymmetric Eu^{3+} site. In BGN:Eu^{3+} crystal, the asymmetry ratio $R(\sim 2.44)$ is lower than those for $\text{BGN:Eu}^{3+},\text{Li}^+$ $R(\sim 4.06)$, suggesting that the symmetry of the Eu^{3+} in co-doped $\text{BGN:Eu}^{3+},\text{Li}^+$ crystals is higher than in BGN:Eu^{3+} . The B_q^k parameters, showed in Table 7 confirm a decreasing of local symmetry of Eu^{3+} ion caused by Li^+ incorporation.

Table 7: B_q^k values for Eu^{3+} calculated with basis on the relaxed lattice of doped BGN:Eu^{3+} .

B_q^k	BGN:Eu^{3+}	$\text{BGN:Eu}^{3+},\text{Li}^+$
B_0^2	0	-51.17
B_1^2	0	-1.03
B_2^2	0	-62.67
B_0^4	3058.14	2922.39
B_1^4	0	-0.91
B_2^4	0	75.64
B_3^4	0	-2.42
B_4^4	1292.30	1275.37
B_0^6	609.85	538.00
B_1^6	0	-11.64
B_2^6	0	-29.41
B_3^6	0	5.08
B_4^6	-1140.93	-1092.43
B_5^6	0	-2.66
B_6^6	0	-43.62

Table 8 shows the energy transition predicted for the Eu^{3+} ion in BGN:Eu^{3+} and $\text{BGN:Eu}^{3+},\text{Li}^+$ crystals, using the crystal field parameters (B_q^k values) from Table 7. The experimental data are also shown for comparison. It is important to point out that the calculated values are predictions using only the B_q^k values obtained with the relaxed lattice surrounding the dopant, without any necessary previous knowledge of the spectra of the real system. The percentage difference between the predicted and the experimental results for

the ${}^5D_0 \rightarrow {}^7F_1$ and ${}^5D_0 \rightarrow {}^7F_2$ transition energies are lower than 3% for both crystals, which shows the reliability of this method to perform this kind of calculation. Another important aspect is the comparison between total splitting of the ${}^5D_0 \rightarrow {}^7F_j (j = 1, 2, 3)$ transitions in BGN:Eu $^{3+}$ and BGN:Eu $^{3+}$,Li $^{+}$. The total splitting in ${}^5D_0 \rightarrow {}^7F_1$ in the BGN:Eu $^{3+}$ is predicted to be 0.1 nm, while in the BGN:Eu $^{3+}$,Li $^{+}$ is 1.7 nm. On the other hand, the predicted total splitting of the ${}^5D_0 \rightarrow {}^7F_2$ transitions is 11.4 nm in the BGN:Eu $^{3+}$ crystal, almost the same to that calculated in Li $^{+}$ co-doped, whose splitting is 12.0 nm. The predicted total splitting of the ${}^5D_0 \rightarrow {}^7F_3$ transitions is 10.4 nm and 9.3 nm in the BGN:Eu $^{3+}$ crystal and Li $^{+}$ co-doped, respectively. In general, it is usually observed an increasing of total splitting in the Li $^{+}$ co-doped crystal. The Li $^{+}$ ion incorporation into BGN:Eu $^{3+}$ crystals also subtly influences the energy level shift and splitting of Eu $^{3+}$ ion, as can be observed in Table 8. Similar results were obtained for ZnS:Tm $^{3+}$,Li $^{+}$ [34].

Table 8: Transition Energies of Eu $^{3+}$ in the BGN:Eu $^{3+}$ and BGN:Eu $^{3+}$,Li $^{+}$ crystals.			
Transition	BGN:Eu $^{3+}$		BGN:Eu $^{3+}$,Li $^{+}$
	Energy Exp. (nm)	Energy Cal. (nm)	Energy Cal. (nm)
${}^5D_0 \rightarrow {}^7F_0$	-	565.8	565.9
		577.5	577.2
${}^5D_0 \rightarrow {}^7F_1$	593	577.6	577.3
			578.5
		592.7	592.9
${}^5D_0 \rightarrow {}^7F_2$	613 640	594.1	594.7
		602.2	603.0
		604.1	603.2
			604.9
${}^5D_0 \rightarrow {}^7F_3$	656		631.4
		631.2	635.2
		635.7	636.6
		636.4	637.1
		640.2	639.2
		641.6	640.7
			641.3

Additionally, the creation of Nb $_{Gd}^{\bullet\bullet}$ defects needed to compensate the charge due to the Li $^{+}$ incorporation also could effectively promote the crystallinity leading to higher oscillating strengths for the optical transitions

[5, 35]. $\text{Nb}_{\text{Gd}}^{\bullet\bullet}$ defects also might act as a sensitizer for the effective energy transfer due to the strong mixing of charge transfer states and, therefore, the enhanced Eu^{3+} emission intensity. The charge compensation defects, generated by the Li^+ incorporation, positively could be related to the morphology and grain size change of particles in $\text{BGN:Eu}^{3+}, \text{Li}^+$ crystals as reported by Yu et al. work [10].

4. Conclusions

We successfully modeled the defects induced by Eu^{3+} and Li^+ dopants in $\text{Ba}_2\text{GdNbO}_6$ perovskite. The calculations indicate that the Eu^{3+} and Li^+ ions preferentially are included into the Gd site, being the Li^+ incorporation compensated by the $\text{Nb}_{\text{Gd}}^{\bullet\bullet}$ antisite. The crystal field parameters B_q^k and the transition energies were calculated for Eu^{3+} in the BGN:Eu^{3+} and $\text{BGN:Eu}^{3+}, \text{Li}^+$ crystals. In the BGN:Eu , a vanishing B_0^2 value indicates that the site occupied by the Eu^{3+} ion is an inversion centre. In the other hand, in the $\text{BGN:Eu}^{3+}, \text{Li}^+$ are observed the non-zero values of B_q^k , which suggest a low symmetry site. An excellent agreement between the predicted and experimental values of the transition energies was obtained showing the reliability of method used, as well as explaining the enhancement mechanism of the luminescence properties in BGN:Eu^{3+} by Li^+ co-doping.

5. Acknowledgement

This work was partially supported by the Brazilian funding agencies CAPES, CNPq, FAPITEC and FAPEMA. C. W. A. Paschoal acknowledges R. Ramesh for all support at Univ. California Berkeley. The authors thank Dr. Julian Gale for allowing us to use the GULP code.

References

- [1] H. K. Yang, K. S. Shim, B. K. Moon, B. C. Choi, J. H. Jeong, S. S. Yi, J. H. Kim, Luminescence characteristic of $\text{YVO}_4 : \text{Eu}^{3+}$ thin film phosphors by Li doping, *Thin Solid Films* 516 (16) (2008) 5577–5581.
- [2] R. F. Qiang, S. G. Xiao, J. W. Ding, W. H. Yuan, C. Q. Zhu, Red emission in B^{3+} – and li^+ -doped $\text{SrAl}_2\text{O}_4:\text{Eu}^{3+}$ phosphor under UV excitation, *Journal of Luminescence* 129 (8) (2009) 826–828.

- [3] J. S. Bae, S. B. Kim, J. H. Jeong, J. C. Park, D. K. Kim, S. H. Byeon, S. S. Yi, Photoluminescence characteristics of Li-doped Y_2O_3 : Eu^{3+} thin film phosphors, *Thin Solid Films* 471 (1-2) (2005) 224–229.
- [4] J. S. Bae, J. H. Jeong, S. S. Yi, J. C. Park, Improved photoluminescence of pulsed-laser-ablated Y_2O_3 : Eu^{3+} thin-film phosphors by Gd substitution, *Applied Physics Letters* 82 (21) (2003) 3629–3631.
- [5] S. S. Yi, J. S. Bae, K. S. Shim, J. H. Jeong, J. C. Park, P. H. Holloway, Enhanced luminescence of Gd_2O_3 : Eu^{3+} thin-film phosphors by Li doping, *Applied Physics Letters* 84 (3) (2004) 353–355.
- [6] G. H. Li, T. Long, Y. H. Song, G. M. Gao, J. J. Xu, B. C. An, S. C. Gan, G. Y. Hong, Preparation and luminescent properties of CaAl_2O_4 : Eu^{3+} , R^{+} ($\text{R}=\text{Li}, \text{Na}, \text{K}$) phosphors, *Journal of Rare Earths* 28 (1) (2010) 22–25.
- [7] L. H. Tian, S. Mho, Enhanced luminescence of SrTiO_3 : Pr^{3+} by incorporation of Li^{+} ion, *Solid State Communications* 125 (11-12) (2003) 647–651.
- [8] H. K. Yang, J. W. Chung, B. K. Moon, B. C. Choi, J. H. Jeong, J. H. Kim, K. H. Kim, Enhanced luminescence properties of Li-doped CaTiO_3 : Pr^{3+} thin films grown by PLD under various lithium ion contents, *Current Applied Physics* 11 (3) (2011) S180–S183.
- [9] Z. W. Liu, Y. L. Liu, J. X. Zhang, J. H. Rong, L. H. Huang, D. S. Yuan, Long afterglow in Pr^{3+} and Li^{+} co-doped CaZrO_3 , *Optics Communications* 251 (4-6) (2005) 388–392.
- [10] C. C. Yu, X. M. Liu, M. Yu, C. K. Lin, C. X. Li, H. Wang, J. Lin, Enhanced photoluminescence of $\text{Ba}_2\text{GdNbO}_6$: $\text{Eu}^{3+}/\text{Dy}^{3+}$ phosphors by Li^{+} doping, *Journal of Solid State Chemistry* 180 (11) (2007) 3058–3065.
- [11] H. S. Jang, D. Y. Jeon, Yellow-emitting Sr_3SiO_5 : Ce^{3+} , Li^{+} phosphor for white-light-emitting diodes and yellow-light-emitting diodes, *Applied Physics Letters* 90 (4) (2007) 041906.
- [12] M. L. Pang, W. Y. Shen, J. Lin, Enhanced photoluminescence of Ga_2O_3 : Dy^{3+} phosphor films by Li^{+} doping, *Journal of Applied Physics* 97 (3) (2005) 033511.

- [13] J. D. Gale, Gulp: A computer program for the symmetry-adapted simulation of solids, *Journal of the Chemical Society-Faraday Transactions* 93 (4) (1997) 629–637.
- [14] J. D. Gale, A. L. Rohl, The general utility lattice program (gulp), *Molecular Simulation* 29 (5) (2003) 291–341.
- [15] J. D. Gale, Gulp: Capabilities and prospects, *Zeitschrift fur Kristallographie* 220 (5-6) (2005) 552–554.
- [16] M. P. Tosi, F. G. Fumi, Ionic sizes + born repulsive parameters in NaCl-type alkali halides .2. generalized, *Journal of Physics and Chemistry of Solids* 25 (1) (1964) 45.
- [17] B. G. Dick, A. W. Overhauser, Theory of the dielectric constants of alkali halide crystals, *Physical Review* 112 (1) (1958) 90–103.
- [18] N. F. Mott, M. J. Littleton, Conduction in polar crystals. i. electrolytic conduction in solid salts, *Transactions of the Faraday Society* 34 (1938) 485–499.
- [19] B. R. Judd, Optical absorption intensities of rare-earth ions, *Phys. Rev.* 127 (3) (1962) 750–761.
- [20] G. S. Ofelt, Intensities of crystal spectra of rare-earth ions, *J. Chem. Phys.* 37 (3) (1962) 511–520.
- [21] O. Malta, Theoretical crystal-field parameters for the YOCl:Eu^{3+} system. a simple overlap model, *Chemical Physics Letters* 88 (3) (1982) 353–356.
- [22] M. V. S. Rezende, M. E. Valerio, R. A. Jackson, Modelling the concentration dependence of rare earth doping in inorganic materials for optical applications: Application to rare earth doped barium aluminate, *Optical Materials* 34 (1) (2011) 109–118.
- [23] B. F. dos Santos Jr., M. V. dos Santos Rezende, P. J. Montes, R. M. Araujo, M. A. dos Santos, M. E. Valerio, Spectroscopy study of $\text{SrAl}_2\text{O}_4\text{:Eu}^{3+}$, *Journal of Luminescence* 132 (4) (2012) 10151020.

- [24] M. V. dos Santos Rezende, P. J. Montes, M. E. Valerio, R. A. Jackson, The optical properties of Eu^{3+} doped BaAl_2O_4 : A computational and spectroscopic study, *Optical Materials* 34 (8) (2012) 1434-1439.
- [25] L. A. Khalam, H. Sreemoolanathan, R. Ratheesh, P. Mohanan, M. T. Sebastian, Preparation, characterization and microwave dielectric properties of $\text{Ba}(\text{B}'_{1/2}\text{Nb}_{1/2})\text{O}_3$ [$\text{B}' = \text{La, Pr, Nd, Sm, Eu, Gd, Tb, Dy, Ho, Y, Yb and In}$] ceramics, *Materials Science and Engineering B-Solid State Materials for Advanced Technology* 107 (3) (2004) 264–270.
- [26] A. Dias, L. A. Khalam, M. T. Sebastian, C. William, C. W. A. Paschoal, R. L. Moreira, Chemical substitution in $\text{Ba}(\text{RE}_{1/2}\text{Nb}_{1/2})\text{O}_3$ ($\text{RE} = \text{La, Nd, Sm, Gd, Tb, and Y}$) microwave ceramics and its influence on the crystal structure and phonon modes, *Chemistry of Materials* 18 (1) (2006) 214–220.
- [27] T. S. Bush, J. D. Gale, C. R. A. Catlow, P. D. Battle, Self-consistent interatomic potentials for the simulation of binary and ternary oxides, *Journal of Materials Chemistry* 4 (1994) 831–837.
- [28] C. Pirovano, M. S. Islam, R. N. Vannier, G. Nowogrocki, G. Mairesse, Self-consistent interatomic potentials for the simulation of binary and ternary oxides, *Solid State Ionics* 140 (2001) 115–123.
- [29] C. W. A. Paschoal, E. M. Diniz, Computer modeling of $\text{Ba}_2\text{RE}^{3+}\text{NbO}_6$ ($\text{RE}^{3+} = \text{rare-earth and Y}$) compounds, *Journal of Physics-Condensed Matter* 21 (7) (2009) 075901.
- [30] C. Catlow, A. Lidiard, M. J. Norgett, Vacancy migration in uranium dioxide, *Journal of Physics C: Solid ...* 435 (1975) 1–5.
- [31] R. Reisfeld, Spectra and energy transfer of rare earths in inorganic glasses, *Struct. Bond.* 13 (1973) 53–98.
- [32] G. Blasse, B. Grabmaier, *Luminescent Materials*, Springer Verlag, Berlin, 1994.
- [33] R. Reisfeld, E. Zigansky, M. Gaft, Europium probe for estimation of site symmetry in glass films, glasses and crystals, *Molecular Physics* 102 (2004) 1319-1330.

- [34] A. Stambouli, S. Hamzaoui, M. Bouderbala, Blue emitting acpel devices based upon ZnS:Tm,Li, Thin Solid Films 283(1996) 204] 283 (1-2) (1996) 204–208.
- [35] C. Misbra, J. Berkowitz, K. Johnson, P. Schmidt, Electronic structure and optical properties of europium-activated yttrium oxide phosphor, Phys. Rev. B 45 (1992) 10902–10906.